International Journal of Minerals, Metallurgy and Materials
Volume 24, Number 10, October 2017, Page 1125
DOI: 10.1007/s12613-017-1503-5

Precipitation analysis of as-cast HK40 steel after isothermal aging

M.L. Saucedo-Muñoz[1)], *A. Ortiz-Mariscal*[1)], *V.M. Lopez-Hirata*[1)], *J.D. Villegas-Cardenas*[2)], *Orlando Soriano-Vargas*[3)], *and Erika O. Avila-Davila*[1)]

1) Instituto Politecnico Nacional (ESIQIE), Apdo. Postal 118-395, Mexico, D.F. 07300

2) Universidad Politecnica, Metepec y Tultitlan Edo. Mex., Mexico

3) Tecnológico de Estudios Superiores de Jocotitlan, Jocotitlan, Edo. Mex., Mexico

(Received: 24 February 2017; revised: 17 May 2017; accepted: 19 May 2017)

Abstract: As-cast HK40 steel was aged at 700, 800, or 900°C for times as long as 2000 h. Microstructural characterization showed that the primary M_7C_3 carbide network contained a substantial content of manganese, in agreement with the microsegregation of manganese calculated by Thermo-Calc using the Scheil–Gulliver module. The dissolution of primary carbides caused the solute supersaturation of austenite and subsequent precipitation of fine $M_{23}C_6$ carbides in the austenite matrix for aged specimens. During prolonged aging, the carbide size increased with increasing time because of the coarsening process. A time–temperature–precipitation diagram for $M_{23}C_6$ carbides was calculated using the Thermo-Calc PRISMA software; this diagram showed good agreement with the experimental growth kinetics of precipitation. The fine carbide precipitation caused an increase in hardness; however, the coarsening process of carbides promoted a decrease in hardness. Nanoindentation tests of the austenite matrix indicated an increase in ductility with increasing aging time.

Keywords: as-cast HK40 steel; carbide precipitation; aging; precipitation simulation

1. Introduction

Heat-resistant cast steels are designed to be used at high temperatures; thus, microstructure degradation may occur after their prolonged service exposure at temperatures greater than 800°C [1–5]. For instance, HK40 steel, ASTM A-351 [6], has been used in the manufacture of different components for the oil, gas, thermal power, chemical, and petrochemical industries [1–9]. These components are sensitive to failure because of creep damage, creep fatigue, σ-phase embrittlement, carburization, thermal shock, or high-temperature corrosion [4]. The microstructural changes that occur during heating of this steel are mainly responsible for most of these failures [2–3,7]. Therefore, several studies have been conducted to describe the microstructural changes in this type of steel [1–5,7–9]. Thermo-Calc [10] has been applied successfully to analyze the microstructural changes in different alloys at their respective service temperatures. Furthermore, Thermo-Calc enables us to calculate the expected phases, as well as their composition, for an alloy system not only in the equilibrium state but also in the non-equilibrium condition using the Scheil–Gulliver equation [10]. That is, the phases formed in the as-cast HK40 steel can also be analyzed using this software. Thermo-Calc PRISMA [11] is a software program based on the Langer–Schwartz (LS) theory and the Kampmann–Wagner numerical (KWN) model; this program has recently been used to analyze the precipitation process of different phases during aging of steels and alloys [12]. This software enables researchers to obtain, for instance, the size, size distribution, number density, and the composition of precipitated phases as well as the time–temperature–precipitation (TTP) diagram. Thus, the use of Thermo-Calc PRISMA would be a good alternative to complement the analysis of precipitation during isothermal aging of HK40 steel.

As previously mentioned, the microstructural changes in aged HK40 steel are closely related to the deterioration of its mechanical properties. Recently, nanoindentation tests [13] have been demonstrated to be a good alternative to follow the change in mechanical properties due to the precipitation

Corresponding author: V.M. Lopez-Hirata E-mail: vlopezhi@prodigy.net.mx

evolution in steels under creep condition. Thus, the purpose of the present work is to analyze the precipitation evolution during isothermal aging at 700, 800, and 900°C for different periods of time and its effect on the mechanical behavior of as-cast HK40 steel.

2. Experimental methodology

The chemical composition of the as-cat HK 40 steel is shown in Table 1. The composition is consistent with the nominal one specified in ASTM standard A-351 [6]. Specimens of approximately 10 mm × 10 mm × 10 mm were cut from the as-cast ingot. These specimens were aged at 700, 800, or 900°C for times up to 2000 h in an electric tubular furnace. The as-cast and heat-treated specimens were prepared metallographically, etched with Kalling's reactant (5 g $CuCl_2$, 100 mL HCl, and 100 mL ethanol), and then observed by both optical light microscopy and scanning electron microscopy (SEM). Energy dispersive X-ray spectroscopy (EDX) was used to determine the chemical composition of some precipitates in the steel specimens. Some specimens were also analyzed by X-ray diffraction (XRD) using Cu K radiation. The size of precipitates was determined from high-resolution SEM micrographs at 20000× magnification using commercial software installed on a personal computer. The Rockwell C hardness was measured for all of the specimens according to the standard procedure using a 1470 N load and a diamond indenter [14]. Some specimens were also tested with a commercialized indentation test machine under a load of 2 mN and for a duration of 12 s.

Table 1. Chemical composition of the HK40 steel wt%

C	Mn	Si	Cr	Ni	S	P	Fe
0.40	1.50	1.60	25.00	20.00	0.03	0.03	Bal.

3. Numerical methodology

The Thermo-Calc software was used to carry out the non-equilibrium analysis of the solidification for HK40 steel based on the Scheil–Gulliver equation [10]. The data used in the calculations included the chemical composition reported in Table 1 and the thermodynamic database for steels [15]. This analysis predicts the phases present in the as-cast HK40 steel as well as the degree of microsegregation in the austenite dendrites. In addition, the Thermo-Calc calculations of the pseudobinary and pseudoternary diagrams are useful for predicting the equilibrium phase after aging of the steel.

The precipitation analysis for the as-cast HK40 steel was carried out using the Thermo-Calc (TC) PRISMA software. The simplified growth model was used in precipitation simulations. The initial chemical composition for the precipitation analysis was assumed to be that corresponding to the maximum microsegregation of the austenite dendritic structures calculated with TC using the Scheil–Gulliver equation. The concentrations of most of the alloying elements were slightly lower than their corresponding concentrations in the steel. The kinetic and thermodynamic data were acquired from the TC databases for steels [11,15]. The molar volumes of the matrix and the precipitate phases for the HK40 steel were also calculated from the TC databases. The reference values of interface energy reported in the literature [16] between the austenite σ-phase and the austenite $M_{23}C_6$ phase were 0.28 and 0.22 J/m^2, respectively. Homogeneous nucleation was assumed for the precipitation simulation in the austenite matrix, which is referred to as "bulk nucleation" in TC-PRISMA.

The TC-PRISMA precipitation module [11] is based on the LS theory and uses the KWN method [12] to simulate the concomitant nucleation, growth, and coarsening of precipitates for multicomponent and multiphase alloy systems. The LS theory enables the time evolution of the particle size distribution, mean radius, and the number density to be predicted by solving the following equations:

$$f_a\left(R^*,t\right)=N_{LS}\frac{b}{\overline{R}_{LS}-R^*} \tag{1}$$

$$\frac{dN_{LS}}{dt}=J-f_a(R^*,t)\frac{dR^*}{dt} \tag{2}$$

$$\frac{d\overline{R}_{LS}}{dt}=v\left(\overline{R}_{LS}\right)+\left(\overline{R}_{LS}-R^*\right)\frac{f_a\left(R^*,t\right)}{N_{LS}}\frac{dR^*}{dt}+\frac{1}{N_{LS}}J\left[R^*(t)\right]\left(R^*+\delta R^*-\overline{R}_{LS}\right) \tag{3}$$

$$\left(c_p-\overline{c}\right)\frac{4\pi}{3}\overline{R}_{LS}^3N_{LS}=\left(c_0-\overline{c}\right) \tag{4}$$

Eq. (1) enables calculation of the apparent size distribution $f_a(R^*,t)$, where R^* is the critical radius and t is time. The LS theory considers the evolution of precipitates with mean radius $\overline{R}_{LS}$ larger than R^*; b is a constant. Eq. (2) enables calculation of the number density N_{LS}, whereas Eq. (3) follows the time evolution of mean radius $\overline{R}_{LS}$ as a function of nucleation rate and growth rate of precipitates, $J[R^*(t)]$ and $v\left(\overline{R}_{LS}\right)$, respectively. δR^* is the variation of critical radius R^*. These equations are solved together with the continuity equation, Eq. (4), where c_p is the precipitate composition, c_o is the matrix composition, and $\overline{c}$ is the mean composition of the alloy.

The critical radius R^*, the nucleation rate $J[R^*(t)]$, and the growth rate $v\left(\overline{R}_{LS}\right)$ are evaluated according to the static and dynamic nucleation and growth theories [12]. In the

case of modified Langer–Schwartz (MLS) theory, the equilibrium solubilities are calculated using the linearized version of the Gibbs–Thomson equation [12]. By contrast, the KWN method [12] uses a numerical algorithm to compute the evolution of size distribution $f(R,t)$ with time. In this case, $f(R,t)$ is subdivided into intervals $[R_{j+1}, R_j]$ and n_j particles. The dissolving particles with $R > R^*$ are considered to belong to the precipitating phase. Thus, the continuous time evolution of $f(R,t)$ is split into discrete interval Δt, which causes small changes in radii R and results in matrix supersaturation. This fact enables us to assume that the nucleation and the growth rates are constant during Δt. Thus, $f(R,t)$ can be calculated reliably. This method accounts for the coarsening process without any special treatment.

4. Results

4.1. As-cast HK40 Steel

The equilibrium pseudobinary Fe–Cr phase diagram was calculated using TC for HK40 steel [14]; the result is shown in Fig. 1. This figure shows the equilibrium phases using the TC nomenclature. In the case of the Cr content of HK40 steel, 25wt%, the liquid phase is present until approximately 1370°C and then a slow cooling induces the formation of the austenite phase, which coexists with the liquid. Further cooling promotes the disappearance of the liquid and the subsequent formation of M_7C_3 carbide. This result suggests that the following eutectic reaction occurs: L → austenite + M_7C_3. As cooling progresses, $M_{23}C_6$ carbide, which is notorious, forms via a precipitation reaction: austenite → austenite + $M_{23}C_6$. The austenite phase accompanied by $M_{23}C_6$ remains present at temperatures less than approximately 1200°C as the M_7C_3 carbide disappears. Finally, the σ-phase is also formed by a precipitation reaction: austenite → austenite + σ. Thus, the expected equilibrium phases are austenite, $M_{23}C_6$, and σ at low temperatures for this steel.

Fig. 2 shows an SEM micrograph of the as-cast HK40 steel; its microstructure consists of austenite phase dendrites along with interdendritic regions composed of a carbide network. The network average size is approximately 25 μm. The XRD pattern of the as-cast specimen is shown in Fig. 3. The XRD peaks correspond to the austenite matrix and M_7C_3 carbides. The presence of these phases is consistent with the predicted phases shown in the plot of temperature versus solid fraction calculated using the Scheil–Gulliver model of TC [10] (Fig. 4(a)). This model assumes that solid diffusion in the solid phase is sufficiently small to be considered negligible and that diffusion in the liquid is sufficiently fast for diffusion to be considered complete [10]. In this diagram, the onset of solidification is marked by point A, with the formation of austenite on the line indicated by B. Point C corresponds to the start of M_7C_3 carbide formation, and point D corresponds to the start of ferrite composed mainly of Fe and Cr. In this analysis, the mass fraction of austenite phase is greater than 0.9 and the mass fraction of M_7C_3 is 0.03. The mass fraction of ferrite is approximately 0.01. The low mass fraction of ferrite appears to be the reason that it was not detected in the XRD pattern in Fig. 3.

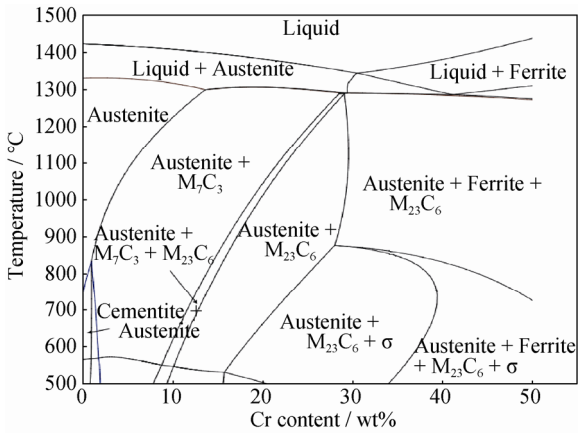

Fig. 1. Equilibrium pseudobinary Fe–Cr phase diagram for HK40 steel.

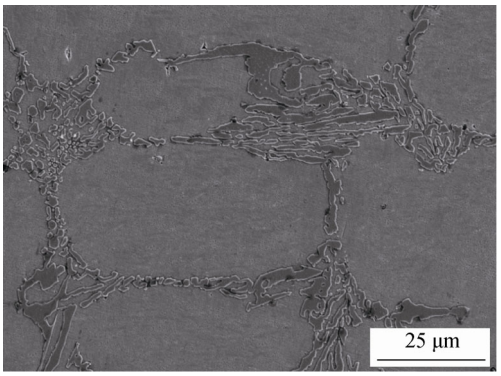

Fig. 2. SEM micrograph of the as-cast HK40 steel.

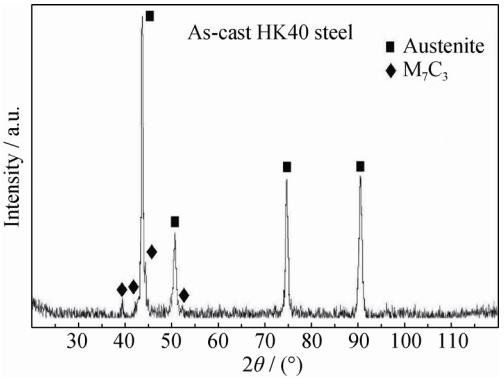

Fig. 3. XRD pattern of the as-cast HK40 steel.

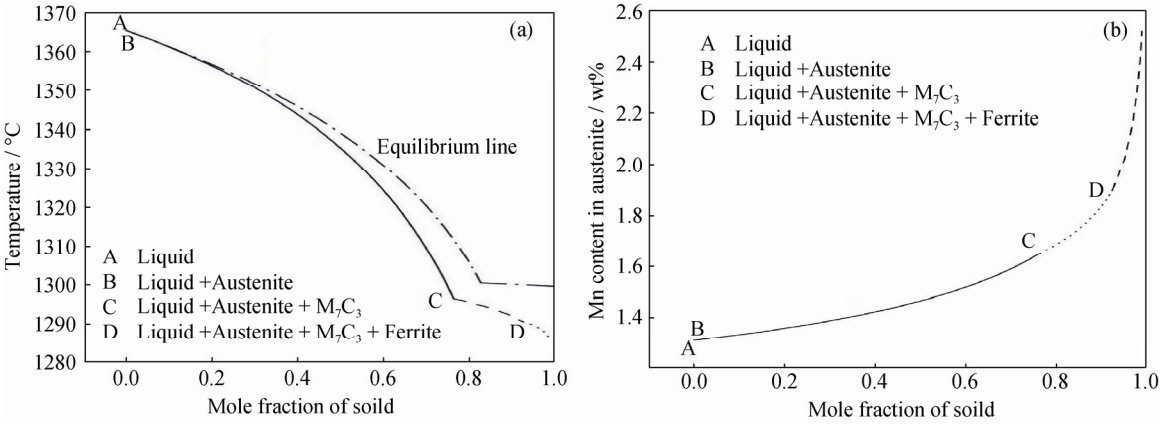

Fig. 4. Plot of temperature vs. solid fraction (a) and Mn content for the austenite phase (b), as determined by Thermo-Calc, in the as-cast HK40 steel.

Fig. 5 shows the SEM image and the corresponding EDX-SEM elemental mapping images for the as-cast specimen. These images confirm the presence of chromium carbides and the existence of nickel in the austenite dendrites. An interesting point is that manganese is also present in the interdendritic zone formed by chromium M_7C_3 carbides and austenite. The chemical element microsegregation of the as-cast alloy was also analyzed using the Scheil–Gulliver model module in TC. The manganese microsegregation from a low to a high content is observed in the austenite dendrite from its center (the first solid to be formed from point A to point C in Fig. 4(b)) to the dendrite extreme (the last part of the solid formed during solidification in this figure). Other elements such as carbon and chromium show the same microsegregation behavior. A remarkable point is that nickel microsegregation is not observed in the austenite dendrite and its concentration in the carbides decreased. Fig. 4(b) also indicates that manganese is concentrated in the network of carbides (the region from point C to D), which is in agreement with the manganese distribution shown in Fig. 5. This carbide network, also known as primary carbides, has been reported [2–3] to be formed by a eutectic reaction, as previously discussed. That is, the liquid phase retains the manganese lost from the dendrite during solidification and then solidifies into a mixture of the austenite phase and M_7C_3 carbides. This process appears to result in manganese being trapped in the interdendritic zone during the solidification process.

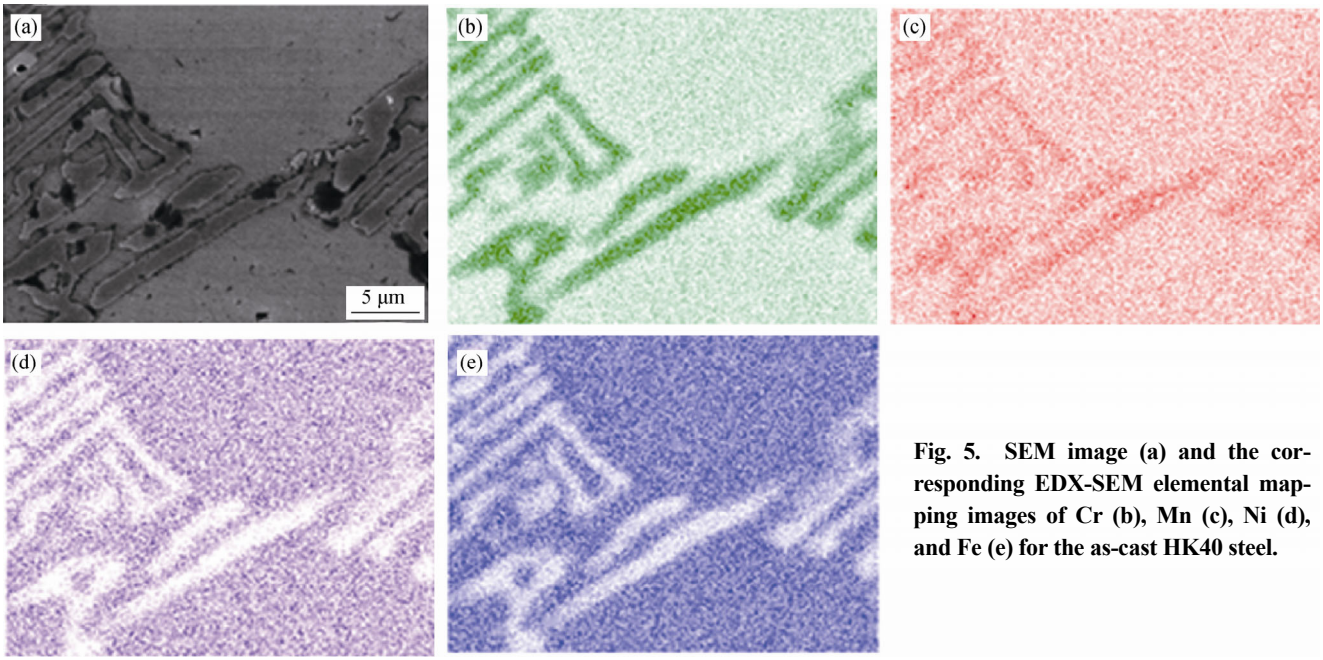

Fig. 5. SEM image (a) and the corresponding EDX-SEM elemental mapping images of Cr (b), Mn (c), Ni (d), and Fe (e) for the as-cast HK40 steel.

4.2. Aged HK40 steel

The evolution of precipitation is shown in Figs. 6(a)–6(c) for the as-cast HK40 steel heated at 800°C for different times. Two events are clearly observed. The first event corresponds to the dissolution of the carbide network, which causes a supersaturation of solutes in the austenite matrix. According to the semiquantitative EDX analysis of the M_7C_3 carbides, as shown in Table 2, the carbon and chromium contents tend to decrease and increase, respectively, with increasing aging time, which suggests carbon supersaturation of the austenite matrix. Furthermore, the chemical composition of the M_7C_3 carbide gradually approaches to the experimental and TC calculated compositions of the $M_{23}C_6$ carbide, as also shown in Table 2. This trend suggests the transformation of $M_7C_3 \rightarrow M_{23}C_6$, and this transformation appears to be the reason why peaks associated with M_7C_3 are not observed in the XRD pattern in Fig. 7. The second event is the precipitation of fine carbides from the solute-supersaturated austenite solution, which are known as secondary carbides. This precipitation event is in agreement with the previously discussed phase transformations in the equilibrium pseudobinary Fe–Cr phase diagram (Fig. 1). The morphology of the secondary carbides is mainly cuboid along with some thin plates that exhibit preferential alignment with the austenite matrix. These morphology and orientation relationships have been reported [17] to occur during the precipitation of $M_{23}C_6$ carbides in the austenite matrix as a result of the low-coherency elastic-strain energy in these crystallographic directions. Furthermore, a cube–cube orientation between these phases has been reported to occur in these steels [17]. In the present work, similar orientation and morphology results were observed in specimens aged at the other two temperatures. The volume fraction of precipitation was slightly higher (9vol%) in the specimens aged at 700°C than in those aged at 800 and 900°C (8vol% and 7vol%, respectively), in good agreement with the TC calculated equilibrium values, which range from 7.4vol% to 7.8vol%. This higher volume fraction for the specimen aged at 700°C is attributable to its greater driving force for precipitation and, thus, its

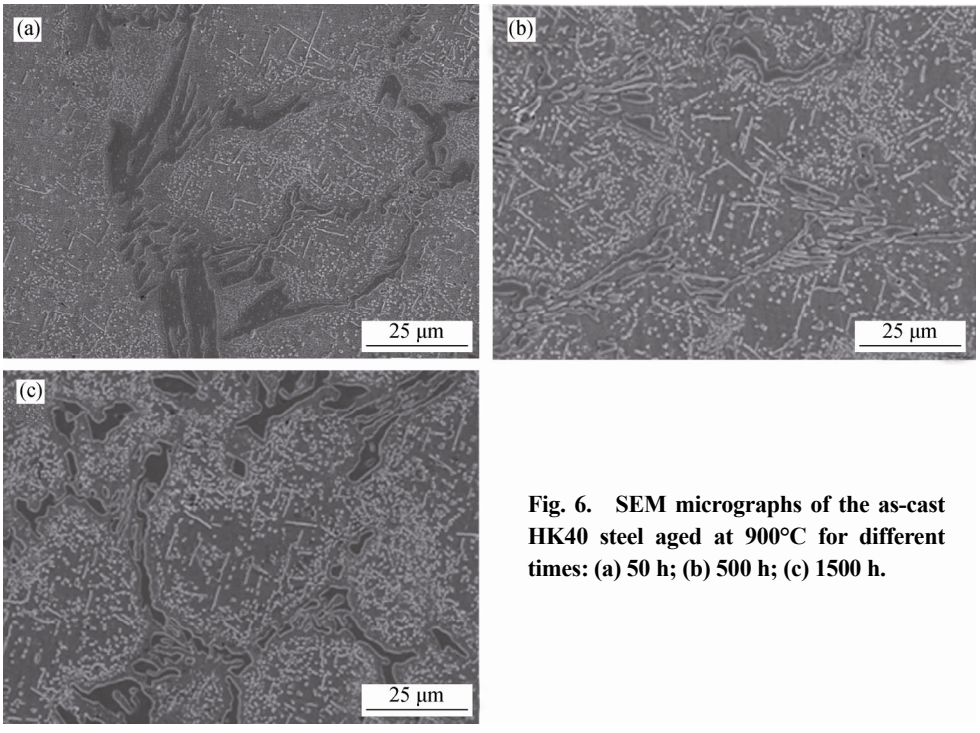

Fig. 6. SEM micrographs of the as-cast HK40 steel aged at 900°C for different times: (a) 50 h; (b) 500 h; (c) 1500 h.

Table 2. Experimental and Thermo-Calc (TC) calculated chemical compositions of carbides wt%

Carbide	Aging time / h	C	Cr	Fe	Ni	Mn
M_7C_3	0	13.7	52.1	27.6	6.6	0.3
	1000	9.7	70.5	17.2	2.6	0.2
$M_{23}C_6$	1000	9.3	66.1	20.1	4.25	0.28
	TC equilibrium value	5.6	78.9	13.5	1.9	0.7

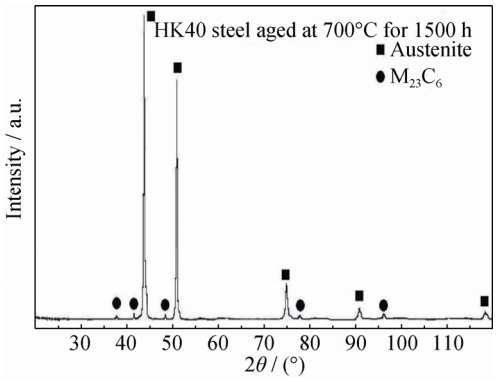

Fig. 7. XRD pattern of the as-cast HK40 steel aged at 700°C for 1500 h.

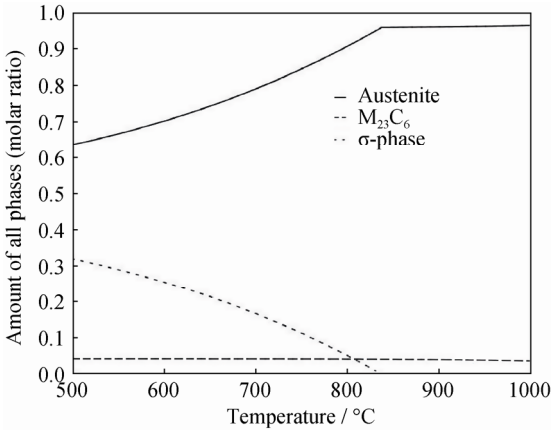

Fig. 8. Amount of all equilibrium phases calculated by Thermo-Calc for the HK40 steel.

faster nucleation rate [12] compared with those of the specimens aged at 800 and 900°C. In addition, SEM observations of the precipitation process indicate that the coarsening of precipitates occurs during aging at all three investigated temperatures. Furthermore, the growth kinetics of precipitate coarsening is faster with increasing aging temperature, which is attributable to an increase in atomic diffusivity [12].

The XRD pattern of the as-cast HK40 steel after aging at 700°C for 1500 h is shown in Fig. 7. This pattern indicates that the precipitated carbide phase in the austenite matrix corresponds to $M_{23}C_6$ carbides; the presence of M_7C_3 carbides was not detected. This result is in good agreement with the TC calculated amounts of equilibrium phases as a function of temperature (Fig. 8), which indicates that the equilibrium phases are mainly $M_{23}C_6$ and austenite for this steel at 800 and 900°C. The σ-phase is also present at 700°C. In addition, the EDX analysis results for the $M_{23}C_6$ precipitates show mainly the presence of chromium, iron, and carbon (Table 2). Furthermore, the SEM analysis of the precipitates indicates that both the cuboid and thin-plate carbides exhibited the same approximate chemical composition, which confirms that both precipitate morphologies correspond to the $M_{23}C_6$ carbides. No formation of the σ-phase was detected in the specimens aged at 700, 800, or 900°C for times as long as 2000 h. This result appears to be related to the higher interfacial energy (0.28 J/m^2) between the σ and austenite phases compared with that between the $M_{23}C_6$ and austenite phases (0.22 J/m^2) [16], which requires a higher driving force to decrease the activation energy for nucleation [12]. Thus, the precipitation of $M_{23}C_6$ carbides precedes that of the σ-phase. This fact also suggests that the nucleation of the σ-phase would be easier at aging temperatures less than 700°C because of an increase in the driving force.

5. Discussion

5.1. Precipitation kinetics

The simulation of precipitation in the aged HK40 steel was conducted using the software TC-PRISMA. The simulation results indicate that the $M_{23}C_6$ precipitates are only formed in the austenite matrix during aging at 700, 800, or 900°C for up to 2000 h, as previously explained. Although the TC software calculated the amounts of equilibrium phases as a function of temperature, as shown in Fig. 8, the results also indicate the presence of σ-phase at 700 and 800°C. This fact is in good agreement with the previously discussed experimental results. TC-PRISMA enables us to calculate the precipitate mean radius variation with time using the KWN method. That is, the mean radius of particles is increased gradually with each Δt increment in time and then the software assesses whether the mean radius is larger than the critical radius for that time. If not, the particles are allowed to continue growing. In the contrary case, the particles are dissolved. This KWN method enables the simultaneous analysis of the nucleation, growth, and coarsening of precipitates. The calculated variation of $M_{23}C_6$ carbide precipitates' radius r with the aging time is shown in Fig. 9 for the HK40 steel aged at 900°C for different interfacial energies between the matrix and the carbides (i.e., 0.15, 0.25, 0.28, and 0.30 J/m^2). Additionally, the experimental results for the carbide equivalent radius are also included in this figure for aging at the same temperature and different times. The mean radius curves corresponding to the interfacial energies of 0.15, 0.25, and 0.28 J/m^2 are in the coarsening stage from 100 to 2000 h because the plot of logarithm of radius vs. logarithm of time produces a straight line with a slope of

approximately 1/3; however; the mean radius curve for 0.30 J/m^2 clearly exhibits a plateau, which indicates that the precipitate growth stops and, thus, that the coarsening stage has not yet been reached [18]. As evident in Fig. 9, the experimental values are closer to the precipitate growth kinetics for the interfacial energy of 0.25 J/m^2, which is in good agreement with the energy values reported in the literature [16]. Thus, this energy value was used in subsequent calculations. Notably, the evolution of the experimental mean radius with time for $M_{23}C_6$ precipitates corresponds to the coarsening stage and follows the modified Lifshitz–Slyosov–Wagner (LSW) theory for diffusion-controlled coarsening [12]. That is, the cube value of the equivalent radius of precipitates shows a linear relation with aging time, in good agreement with the exponent of 1/3 calculated by the TC-PRISMA simulation.

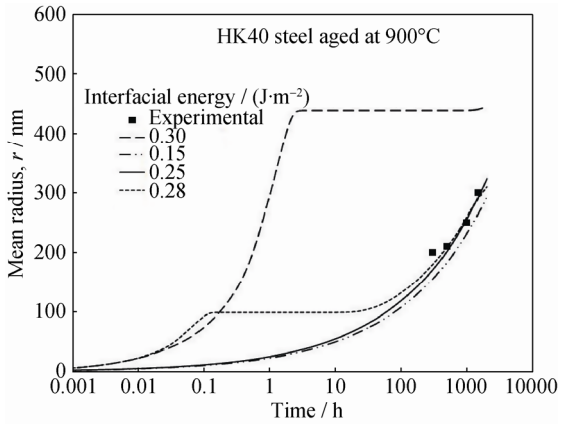

Fig. 9. Plot of mean radius *r* versus aging time *t* calculated by TC-PRISMA.

The TTP diagram calculated by TC-PRISMA is shown in Fig. 10 for the precipitation of the $M_{23}C_6$ carbide and σphases in the austenite matrix. The start curve for bulk nucleation was calculated for a minimum volume fraction of 0.001. The fastest growth kinetics of precipitation occurs during aging at approximately 875°C. According to the TTP diagram of this steel, the growth kinetics of precipitation is faster for aging at 900°C than at 800 or 700°C. The slowest kinetics corresponds to the aging at 700°C. Fig. 10 also shows the micrographs corresponding to the precipitation evolution in the as-cast HK40 steel aged at 700, 800, or 900°C for 50, 150, or 1500 h. The largest experimental precipitate size and the lowest precipitate volume fraction correspond to aging at 900°C. Conversely, the smallest size and highest volume are for aging at 700°C. This behavior is attributable to the higher force driving for nucleation during aging at 700°C, which promotes a higher nucleation rate and, thus, a higher volume fraction of precipitates, whereas the slower atomic diffusion causes slower growth-coarsening kinetics, resulting in a smaller precipitate size. The contrary effect—faster diffusion and coarsening occurs in the case of aging at 900°C.

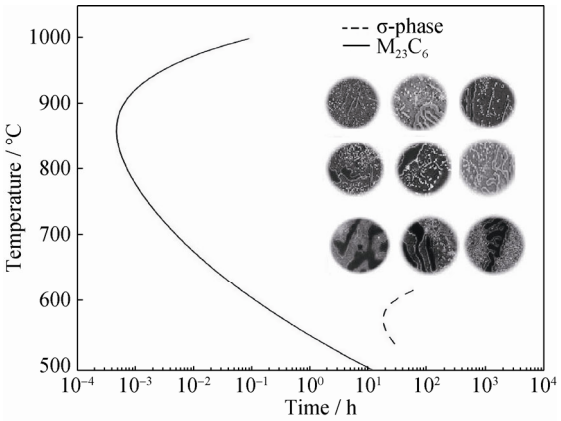

Fig. 10. TTP diagram calculated by TC-PRISMA for $M_{23}C_6$ precipitation.

The start curve for the σphase precipitation is located at lower temperatures, 550 to 650°C, and corresponds to times longer than 20 h. In the calculated TTP diagram, the interfacial energy was assumed to be 0.1 J/m^2; however, the increase in interfacial energy results in a shift of the start curve to longer times. The calculated volume fraction of the σphase is approximately 1.5% for aging at 600°C for 2000 h. The calculated TTP diagram suggests that the start of the σ-phase precipitation would occur at aging times longer than 2000 h at 700°C.

5.2. Age hardening

The evolution of the Rockwell C hardness as a function of aging time at 700, 800, or 900°C is shown in Fig. 11. An increase in hardness with time is observed in specimens for the three aforementioned aging temperatures, which is attributed to the fine size of $M_{23}C_6$ carbide precipitates. Nevertheless, the hardness for specimens aged at 900°C shows a rapid decrease in hardness for shorter times as a result of its faster coarsening process, as previously described. By comparison, the specimens heated at 700 or 800°C exhibited a decrease in hardness after longer aging times compared with the hardness of the specimen heated at 900°C. In addition, aging at 700°C promoted greater precipitation hardening because of the finer precipitation at this temperature. The behavior of precipitation hardening is in good agreement with the growth kinetics of $M_{23}C_6$ precipitation, as shown in Fig. 10.

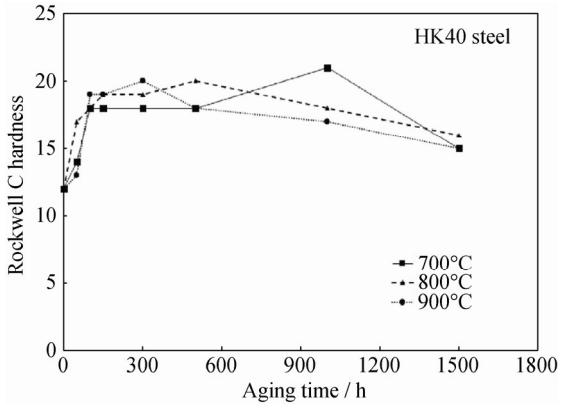

Fig. 11. Plots of Rockwell C hardness versus aging time for the HK40 steel at 700, 800, and 900°C, respectively.

Fig. 12 shows the plots of load versus displacement of the nanoindentation test for the austenite matrix in the as-cast HK40 steel aged at 800°C for 0 (as-cast), 50, 500, or 1500 h. The ductility (softness) of the austenite matrix increases with the aging time despite the precipitation hardening, as shown in Fig. 11. The increase in ductility of the matrix appears to be associated with the loss of different solutes from the austenite matrix during the different stages of the precipitation process: nucleation, growth, and coarsening. The nanoindentation results for the specimens aged at 900°C show the same increase in ductility for shorter aging times, which is associated with the faster growth kinetics of precipitation at this temperature. Nevertheless, the nanoindentation results show no clear tendency in the case of the specimen aged at 700°C, likely because of the higher volume fraction of fine precipitates dispersed in the austenite matrix.

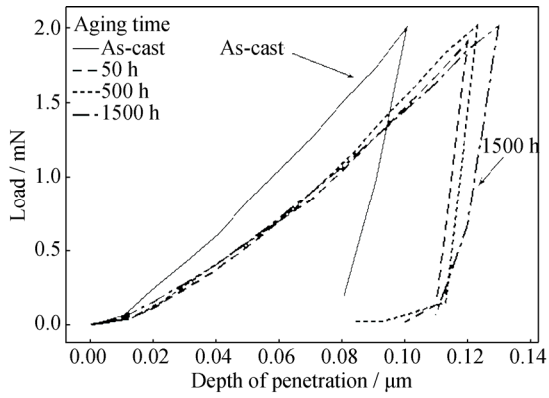

Fig. 12. Plots of load versus displacement for the HK40 steel aged at 800°C for different times.

6. Conclusions

Precipitation analysis was carried out during the isothermal aging of the as-cast HK40 steel. The conclusions are summarized as follows:

(1) The experimental and TC analyses of the aging process at 700, 800, and 900°C for times up to 2000 h in the as-cast HK40 steel show that the primary M_7C_3 carbide network was not only composed of iron, chromium, and carbon, but also manganese. The primary carbides were dissolved at the early stages of aging, which caused carbon solute supersaturation of the austenite matrix; thus, increasing aging time promoted the precipitation of secondary $M_{23}C_6$ carbides. The chemical composition of M_7C_3 changed during precipitation, and it became close to that of $M_{23}C_6$.

(2) The TC-PRISMA calculated TTP diagram for $M_{23}C_6$ carbides exhibited good agreement with the experimental precipitation growth kinetics.

(3) The fine precipitation induced an increase in hardness with time, and prolonged aging caused the coarsening of precipitates, which promoted a decrease in hardness with increasing aging time.

(4) The loss of solute content in the austenite matrix during precipitation contributed to the increase in ductility, as detected in the nanoindentation tests.

Acknowledgements

The authors wish to thank financial support from SIP-BEIFI-IPN and CONACYT.

References

[1] A.A. Kaya, P. Krauklis, and D.J. Young, Microstructure of HK40 alloy after high temperature service in oxidizing/carburizing environment: I. Oxidation phenomena and propagation of a crack, *Mater. Charact.*, 49(2002), No. 1, p. 11.

[2] J.W. Liu, D.L. Jiao, and C.P. Luo, Microstructural evolution in austenitic heat-resistant cast steel 35Cr25Ni12NNbRE during long-term service, *Mater. Sci. Eng. A*, 527(2010), No. 10-11, p. 2772.

[3] S. Haro R., D. Lopez L., A. Velasco T. and R. Viramontes B., Microstructural factors that determine the weldability of a high Cr-high Si HK40 alloy, *Mater. Chem. Phys*., 66(2000), No. 1, p. 90.

[4] A.M. Babakr, A.A. Al-Ahmrai, K. Al-Jumayiah, and F. Habiby, Failure investigation of a furnace tube support, *J. Fail. Anal. Prev*., 9(2009), No. 1, p. 16.

[5] A.A. Kaya, Microstructure of HK40 alloy after high-temperature service in oxidizing/carburizing environment: II. Carburization and carbide transformations, *Mater. Charact*., 49(2002), No. 1, p. 23.

[6] ASTM Standard, ASTM A351/A351M–03, *Standard Speci-*

fication for Casting, Austenitic, Austenitic-Ferritic (duplex), for Pressure-Containing Parts, ASTM, 2004.

[7] O. Coreño-Alonso, A. Duffus-Scott, C. Zánchez-Cornejo, J. Coreño-Alonso, F. Sánchez-de Jesús, and A. Bolarín-Miró, On the effect of σ-phase formation during metal dusting, *Mater. Chem. Phys*., 84(2004), No. 1, p. 20.

[8] L.H. de Almeaida, A.F. Ribeiro, and L.L. May, Microstructural characterization of modified 25Cr–35Ni centrifugally cast steel furnace tubes, *Mater. Charact*., 49(2003), No. 3, p. 219.

[9] M. Whittaker, B. Wilshire, and J. Brear, Creep fracture of the centrifugally-cast superaustenitic steels, HK40 and HP40, *Mater. Sci. Eng. A*, 580(2013), No. 9, p. 391.

[10] J.O. Andersson, T. Helander, L. Höglund, P.F. Shi, and B. Sundman, Thermo-Calc & DICTRA, computational tools for materials science, *Calphad*, 26(2002), No. 2, p. 273.

[11] Thermo-Calc Prisma software [tcfe7.tdb and mobFe2.ddb data] version 2016b, Sweden, 2016.

[12] G. Kostorz, *Phase Transformations in Materials*, Wiley-VCH, Germany, 2001, p. 311.

[13] W.C. Oliver and G.M. Pharr, An improved technique for determining hardness and elastic modulus using load and displacement sensing indentation experiments, *J. Mater. Res*., 7(1992), No. 6, p. 1564.

[14] ASTM Standard, ASTM E18-02, *Standard Test Methods for Rockwell Hardness and Rockwell Superficial Hardness of Metallic Materials*, ASTM, 2004.

[15] Thermo-Calc software [tcfe7.tdb data] version 2016b, Sweden. 2016.

[16] T. Sourmail, Precipitation in creep resistant austenitic stainless steels, *Mater. Sci. Technol.*, 17(2001), No. 1, p. 1.

[17] G.R. Kegg and J.M. Silcock, The shape of $M_{23}C_6$ particles, *Scripta Metall*., 6(1972), No. 11, p. 1083.

[18] K.G.F. Janssens, D. Raabe, E. Kozeschnik, M.A. Miodownik, and B. Nestler, *Computational Material Engineering*, Elsevier, UK, 2007, p. 179.